Development of a Physically-Based Creep Model Incorporating Eta Phase Evolution for Nickel Base Superalloys

Final Scientific/Technical Report

US Department of Energy, National Energy Technology Laboratory, Pittsburgh

Grant Number DE-FE0027822

Grant Period: 8/15/2016 – 2/15/2021

Program Manager: Omer Bakshi

Walter W. Milligan, Principal Investigator
Professor, Materials Science and Engineering
Michigan Technological University
1400 Townsend Drive
Houghton, MI 49931

(906) 487-2015, milligan@mtu.edu

DUNS: 065453268

Collaborators:

Paul G. Sanders, Calvin L. White, Ninad Mohale (PhD Student)
Michigan Technological University

John P. Shingledecker
Electric Power Research Institute, Charlotte, NC

May 14, 2021

Acknowledgement

This research was funded by the US Department of Energy, Fossil Energy Program, Grant Number DE-FE0027822. The investigators gratefully acknowledge the financial support, as well as the collaboration with the Program Manager Omer Bakshi and his colleague Vito Cedro at the National Energy Technology Laboratory in Pittsburgh, PA.

Disclaimer

Development of a Physically-Based Creep Model Incorporating Eta Phase Evolution for Nickel Base Superalloys

Contents

Executive Summary

Nickel-base superalloys that are in service for long periods of time in fossil energy powerplants have microstructures that evolve with time. The strengthening gamma prime phase coarsens, and in some alloys, a new phase (eta) forms at grain boundaries, and its effect on creep performance is not fully understood.

In order to study the effects of eta phase on the creep of a typical nickel-base superalloy, Alloy 263 was aged for 1,000 hours at 1123 K. This resulted in precipitation of eta phase at and near the grain boundaries, reduction of the volume fraction of gamma prime, and increased gamma prime precipitate size. The Aged 263 was creep tested at 973, 1023 and 1073 K at various stresses, along with the Standard Alloy 263, and an experimental alloy that contains only eta phase and no gamma prime, with a chemical composition close to that of Alloy 263.

The creep performance of the Standard 263 was superior at all conditions, with the exception of creep ductility, which was substantially elevated in the Aged 263 and the eta alloy. The enhanced creep ductility in the aged microstructure is proposed to be related to the grain boundary regions being denuded in gamma prime, and also the presence of rich matrix dislocation sources in the eta/gamma interfaces.

Deformation mechanisms were determined via transmission electron microscopy. The dominant mechanism changed from traditional precipitate shearing at 973 K to a combination of traditional and partial-dislocation shearing at 1023 K to climb-assisted precipitate by-pass at 1073 K.

Based on these mechanisms, an existing physically-based creep model was modified to predict steady-state creep rates in both the Standard and Aged 263. The presence of the eta phase was not addressed explicitly, but indirectly through the change in the gamma prime volume fraction and size. The model was very successful at 973 K, moderately successful at 1073 K, and a complete failure at 1023 K.

The reason for the failure at 1023 K was that the physically-based creep model for shearing is based on traditional precipitate shearing, and so the onset of partial dislocation-based shearing and the accompanying stacking faults would require a completely new model formulation.

1. Introduction

Wrought nickel-base alloys such as INCONEL® 740/740H and NIMONIC 263 are being considered for high-temperature, high-efficiency electric power generation facilities. With few exceptions, these alloys are strengthened by the gamma prime phase, designated γ', and based on the $Ni_3Al/L1_2$ structure. During extended times at operating temperatures, other phases can form, and many of these phases are considered to be detrimental to performance. One such phase that forms in these types of alloys is the eta phase, designated η, and based on the $Ni_3Ti/D0_{24}$ structure [1]. The η phase is known to form at the expense of the γ' strengthening phase at long service times. Examples of this phase formation are shown in Figure 1 from a study by Unocic et al. in IN740 [2].

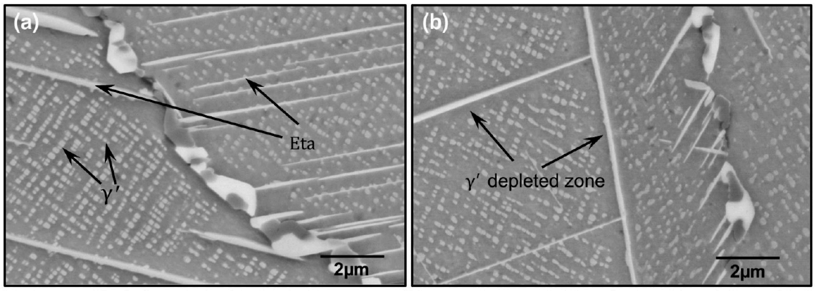

Figure 1. Development of η phase plates in IN740 after 23,000 hours at 1023 K (750°C) [2]

It has been speculated that this development of η phase might be deleterious to creep performance. Not only does the η phase reduce the volume fraction of the γ' strengthening phase, but it also occurs at grain boundaries in sharp shapes, perhaps leading to enhanced cavitation and crack initiation.

However, in the available studies of the effects of η phase on performance in the literature, there is no broad agreement that η phase is detrimental, as summarized in Table 1.

Table 1. Summary of literature observations of η phase on performance of typical alloys

Alloy [Reference]	**Temperatures, K**	**Observations**
N263 [3]	1073	Reduced creep ductility
N263 [4]	1100	Detrimental to strength and ductility
IN740 [5]	1023-1123	Reduced impact toughness
IN740 [6]	1090	Reduced strength, limited ductility
IN740 [7]	1023-1123	Reduced creep ductility above 7% η
IN740 [1]	*1023*	*Not detrimental to creep*
IN740 [2]	*1023*	*Not detrimental to creep*

The studies summarized in Table 1 varied significantly in stress levels and durations of the tests, as well as in the η volume fraction. Furthermore, none of these studies incorporated detailed evaluation of the effects of η phase formation on constitutive behavior during creep. The present study was undertaken to clarify the effects of η phase formation on the creep performance, and in particular the constitutive behavior, of these alloys.

2. Project Goals

The primary objective of this work is to develop a physically based creep model for Nimonic 263 that synthesizes known creep behavior based on γ'strengthening with a new understanding of the effects of η phase on creep performance at long service times in fossil energy power plants.

In all previous studies, the η phase evolved during the creep tests after long service times at elevated temperatures. Other microstructural features also evolved during these creep tests that may have confused the interpretation of the η phase effects. In order to clarify the effects of the η phase on creep performance of Alloy 263, three different microstructures were produced by alloy design and heat treatment prior to creep testing:

1. "Standard" Alloy 263 containing only γ'.
2. "Aged" Alloy 263 containing both γ' and η.
3. An experimental alloy similar to Alloy 263 which contains only η and no γ'.

Thus, three different microstructures containing 3 different distributions of γ' and η were produced and creep tested. Some of the creep testing on the standard alloy was previously conducted at The Electric Power Research Institute (EPRI).

3. Materials and Microstructures

The compositions of Alloy 263 and the experimental "Alloy 20" are given in Table 2.

Table 2. Chemical compositions of the alloys (weight pct)

	Ni	Co	Cr	Al	Fe	Mo	Mn	Si	Ti	Nb	W	Ta	V	C
263	Bal	20	20	0.6	0.7	6	0.6	0.4	2	0	0	0	0	0.06
20	Bal	21	21	0.14	0.5	0	0.4	0.2	2.8	2	2	1	0.85	0.07

Alloy 20 was designed in a previous study to be similar in composition to Alloy 263, but to contain only η and no γ' [8,9]. Its microstructure after aging at 1123 K is shown in the TEM and SEM images in Figure 2, where only plate-like η phase is present in a Widmanstätten microstructure [8,9].

The "standard" Alloy 263 is a polycrystalline, wrought alloy containing approximately 15% γ', along with grain boundary carbides. The γ' in this alloy is spherical, and approximately 40 nm in diameter after solution treating, quenching and aging.

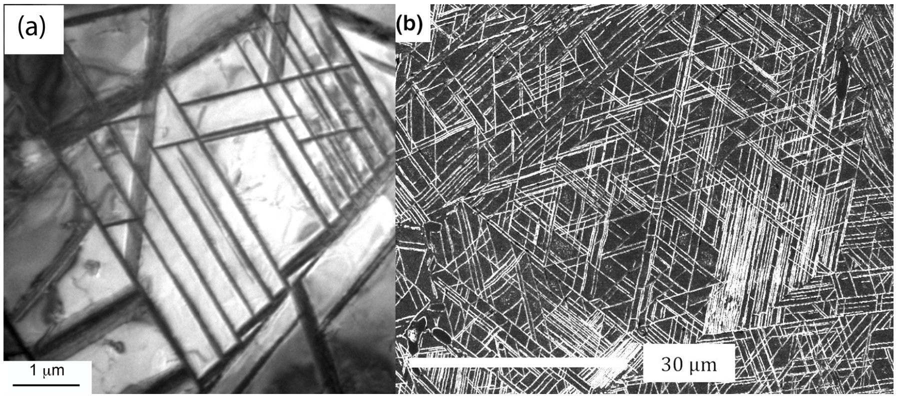

Figure 2: Microstructures of the experimental Alloy 20 after aging at 1123 K, designed using computational thermodynamics to contain only η and no γ' [8,9]. η plates in a Widmanstätten microstructure are the dominant features. (a) TEM micrograph of Alloy 20. (b) SEM micrograph of an alloy with a very similar composition.

In order to generate microstructures containing η and γ' prior to creep testing, aging experiments were conducted for extended times at temperatures between 1023 K (750°C) and 1173 K (900°C). These temperatures were chosen based on an Isothermal Transformation diagram for η and γ' precipitation that was proposed for Alloy 263 by Zhao et al. [10]. The results of these experiments were as follows:

1. There was very little η precipitation at 1023 K (750°C) at times up to 7,000 hours.
2. 1173 K (900°C) was at or near the η and γ' solvus temperatures, as very little η or γ' was present upon quenching from 1173 K.
3. Useful microstructures containing η and γ' could be produced at 1073 K (800°C) and 1123 K (850°C), as explained below.

Figure 3 shows an SEM micrograph of an Alloy 263 specimen that had been aged at 1123 K (850°C) for 1,000 hours. This micrograph illustrates the polycrystalline structure of the alloy, along with the spherical γ' precipitates in the centers of the grains, and plate-shaped η

precipitates near the grain boundaries and protruding into the grains. Note the similarities between this structure and that shown in Figure 1, developed in a similar alloy during creep after 23,000 hours at 1023 K.

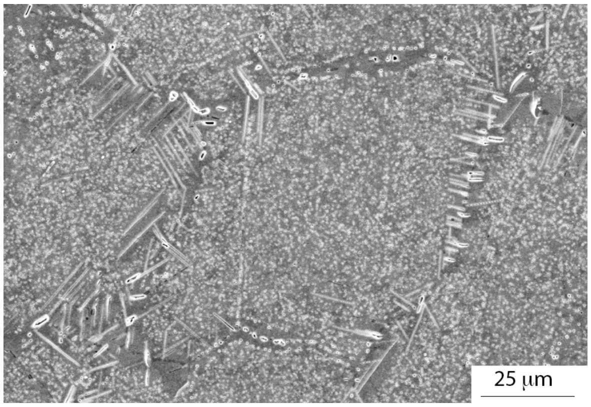

Figure 3: SEM micrograph of Alloy 263 after aging at 1123 K (850°C) for 1,000 hours. Note presence of plate-shaped η precipitates *near grain boundaries.*

In addition to the precipitation of η, heat treatment of Alloy 263 at these times and temperatures coarsens the γ', and some of the γ' near the grain boundaries dissolves at the expense of the of η growth. Figure 4 shows the evolution of η volume fraction and γ' precipitate diameter during aging at these temperatures. The goal of the heat treatments was to obtain a microstructure with a substantial volume fraction of η while limiting the γ' coarsening. Unsurprisingly, these goals turned out to be mutually exclusive; the compromise choice for the (η+γ') microstructure is the one shown in Figure 3, aged at 1123 K for 1,000 hours. This microstructure contains about 6% η by volume, and the remaining γ' precipitates have coarsened to a diameter of around 115 nm. The microstructure shown in Figure 3, developed by aging the standard N263 alloy at 850°C for 1,000 hours, will be referred to in the remainder of this report as the “Aged 263” alloy containing both η and γ'. The other two materials that were tested will be referred to as “263” for the standard N263 alloy, and “η” or “η alloy” (Figure 2.)

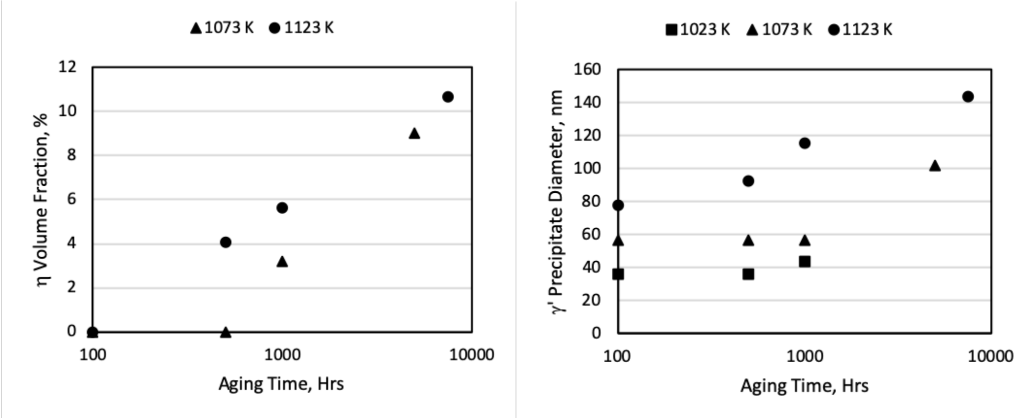

(a) (b)

Figure 4. Microstructural evolution of Alloy 263 with aging times. (a) Volume fraction of η *phase. (b) Diameter of* γ' *precipitates.*

4. Results – Creep Testing

Creep tests were conducted on all three alloys at 973, 1023 and 1073 K (700, 750 and 800^{o}C) at a variety of stresses. The creep curves are presented in Figures 5-7.

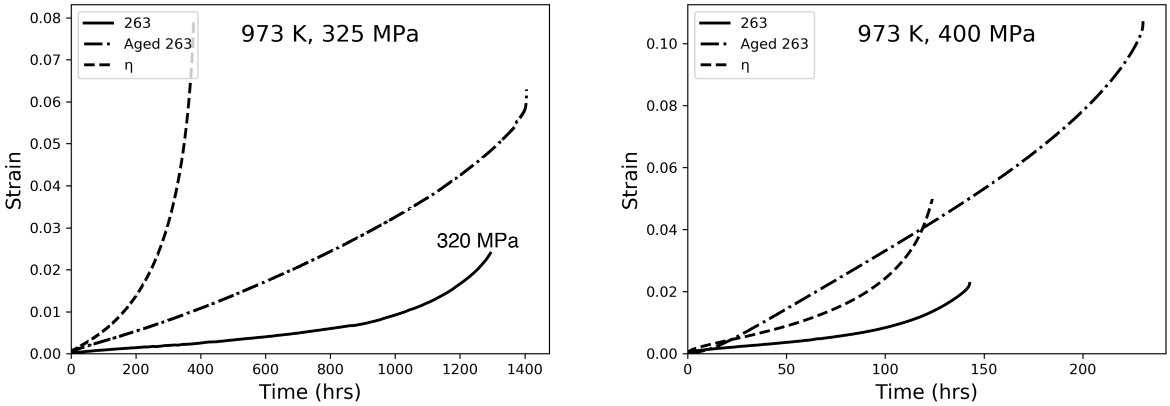

Figure 5. Creep curves obtained at 973 K (700^{o}C).

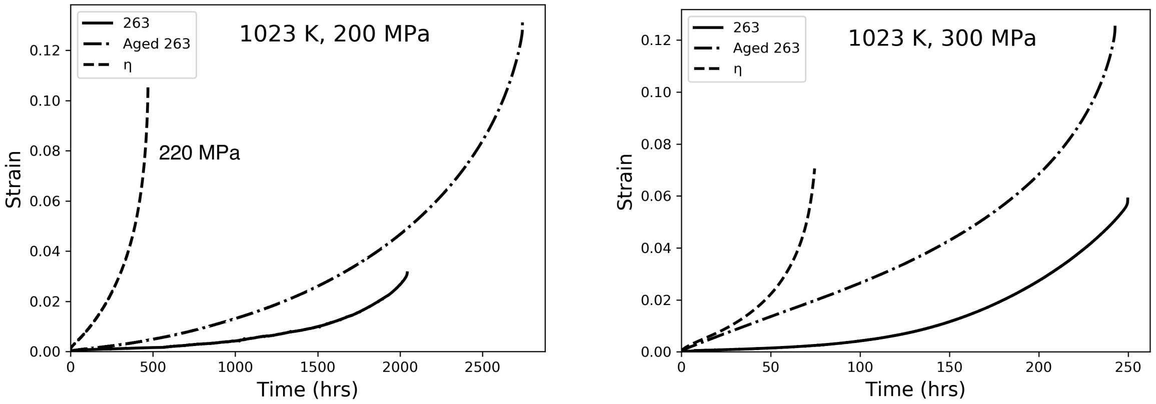

Figure 6. Creep curves obtained at 1023 K (750^{o}C).

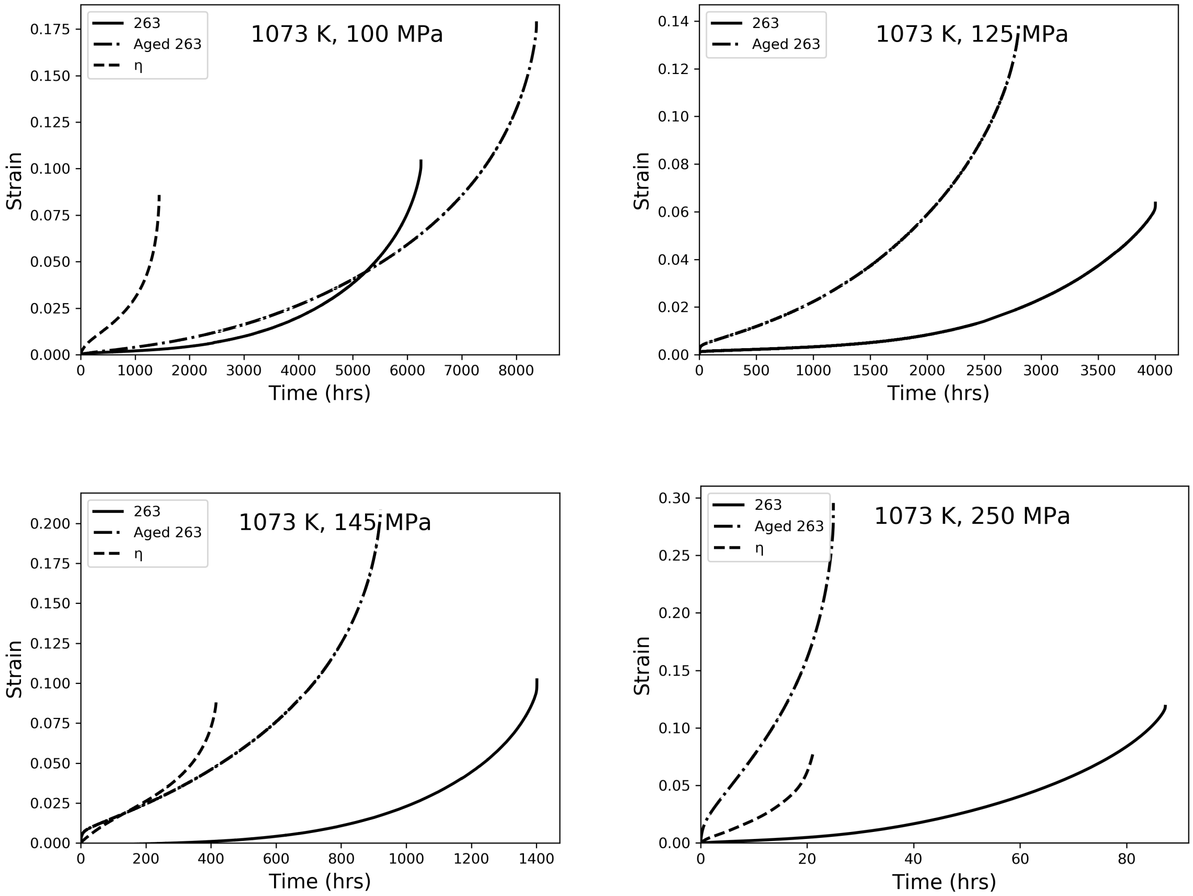

Figure 7. Creep curves obtained at 1073 K (800ºC).

Inspection of the creep curves leads to the following conclusions:

1. The Standard 263 alloy had the lowest creep rates in primary and secondary creep at all temperatures and stresses. In most, but not all cases, the η alloy has the highest creep rates, with the Aged 263 falling in the middle.
2. The η alloy always had the shortest creep rupture life.
3. The creep ductility of the Aged 263 was always substantially higher than that of the Standard 263. The creep ductility of the η alloy was superior to the Standard 263 at 973 and 1023 K, and was approximately equal to the Standard 263 alloy at 1073 K.
4. The Aged 263 had the best creep rupture lives at 973 and 1023 K, as well as at the lowest stress of 100 MPa at 1073 K. At higher stresses at 1073 K, the Standard 263 had the highest creep rupture lives.

5. Results – Deformation Mechanisms

Deformation mechanisms were studied by transmission electron microscopy (TEM). Thin foils were prepared by electropolishing 3 mm disks in a solution of 5% perchloric acid, 35% ethylene glycol butyl ether, and 60% methanol at -40°C and 20 V. TEM studies were conducted in an FEI Titan Themis, mainly in traditional brightfield mode.

In order to develop a physically-relevant model of the creep process, it is necessary to determine the rate-limiting deformation mechanisms during creep. In nickel-base superalloys, the strengthening γ' phase must be overcome by dislocations in order for creep strain to occur. There are three basic ways that the precipitates could be overcome by dislocation motion:

1. Shearing of the precipitates, either by antiphase boundary (APB) coupled ½<110> dislocation pairs which glide through the matrix and the precipitate, or by <112> partial dislocations which may leave remnant stacking faults behind.
2. Climb-assisted by-pass of the precipitates, whereby a dislocation which is gliding in the matrix comes up against the interface, and moves up the interface by diffusion-controlled climb, and finally escapes the precipitate obstacle after climbing up and around it.
3. Orowan looping.

In creep of these types of alloys in the temperature range of interest in this study, the first two are normally the ones that are observed. Figure 8 shows schematic diagrams of the dislocation precipitate interactions in both of these cases.

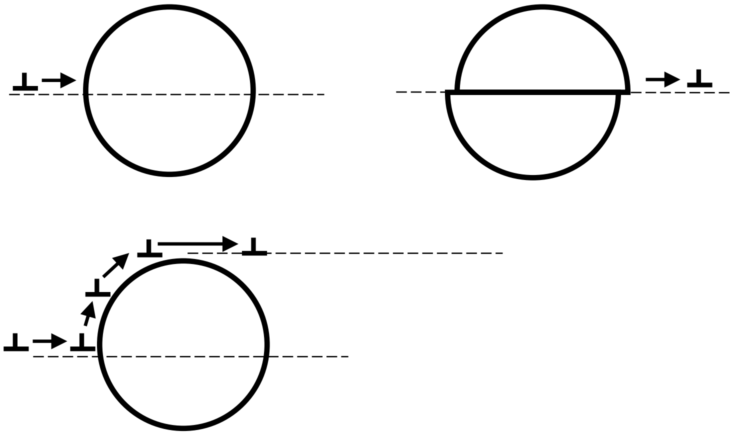

Figure 8. Fundamental deformation mechanisms in nickel-base superalloys. ***Top:*** *Dislocations shear the strengthening γ' precipitates.* ***Bottom:*** *Dislocations by-pass the strengthening γ' phase, by climb and glide in the interface between the matrix and the γ'. By-pass is controlled by diffusion during climb of edge-component dislocations.*

The temperature range over which the tests were conducted in this study typically bounds a transition from shearing (from 0 K through somewhere around 1050 K depending on alloy, microstructure and strain rate) to by-pass at higher temperatures and lower strain rates.

5(a) Highest Temperature – 1073 K (800^{o}C)

The deformation behavior at this temperature is the most straightforward and is consistent with the literature on similar alloys. For both the Standard 263 and the Aged 263, deformation at all stresses occurred by climb-assisted by-pass.

This is ascertained in post-mortem TEM analysis by observing that the dislocations are almost all in the matrix, pushed up against the matrix/precipitate interface. The dislocations appear to wind around the precipitates, and in some cases leave loops behind that are similar to Orowan loops. Dislocation debris is rarely evident inside the precipitates, unlike in shearing, where it is very likely that some dislocations would be left inside the precipitates as the test ended, either in the act of shearing, or pinned due to a cross-slip event or other interaction. If the precipitates are small enough that much of the interface is contained in the thickness of the foil, one can also observe the curvature of the dislocation in the interface due to the mechanism shown in Figure 8 (bottom). In cases where there is doubt, stereo-pair imaging can be useful to determine if the dislocations are actually inside the precipitates, or in the interface. This was not determined to be necessary in this study.

Figure 9 shows a typical example in the Standard 263 tested at 1073 K (800^{o}C) and 250 MPa. There are many long dislocations trapped in the foil, which is approximately 100 nm thick. Some of the dislocations are around 500 nm long, indicating that the primary slip plane is very close to the plane of the micrograph. The dislocations are in the matrix, pushed up against interfaces, and with some leaving loops behind. In the only cases where it appears that dislocations may be in the precipitates, there is actually a change in curvature that is close to the precipitate radius indicating that it is actually in the interface, as in the arrows in Figure 9.

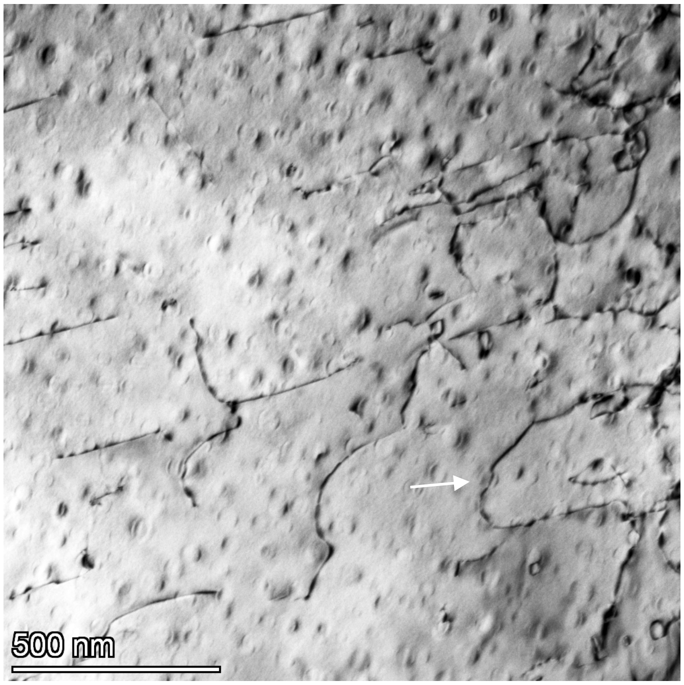

Figure 9. Climb-assisted by-pass in Standard 263, 1073 K and 250 MPa. <111> ***g****. Dislocations are mainly in matrix and pushed up against interfaces. At arrow, top interface is included in thickness of the specimen and the dislocation is bowing up as it lies in the interface in the act of by-pass.*

In the Aged 263 alloy at 1073, a few new features were evident, as shown in Figure 10. First, there were some stacking faults present in the precipitates (the fringed pattern running vertically inside some of the γ' precipitates); second, there is an η plate in the top-left of the micrograph; third, near the plate there is a γ' denuded zone containing matrix dislocations. Most of the dislocations are in the matrix, and wrapped around the precipitates. Very rarely was a stacking fault observed in the Standard 263 alloy at this temperature, and this implies that as the precipitate size increases, there may be a higher propensity for <112> partial dislocation shearing. It should be kept in mind that the stacking faults, though visually impressive, are often the result of only one partial dislocation passing through a particle.

Finally, there is evidence of η plates/interfaces acting as dislocation sources as the matrix dislocations are connected to the η plates in Figure 10. This was observed as well in the η only alloy at this temperature as discussed below. This is a possible source of improved creep ductility.

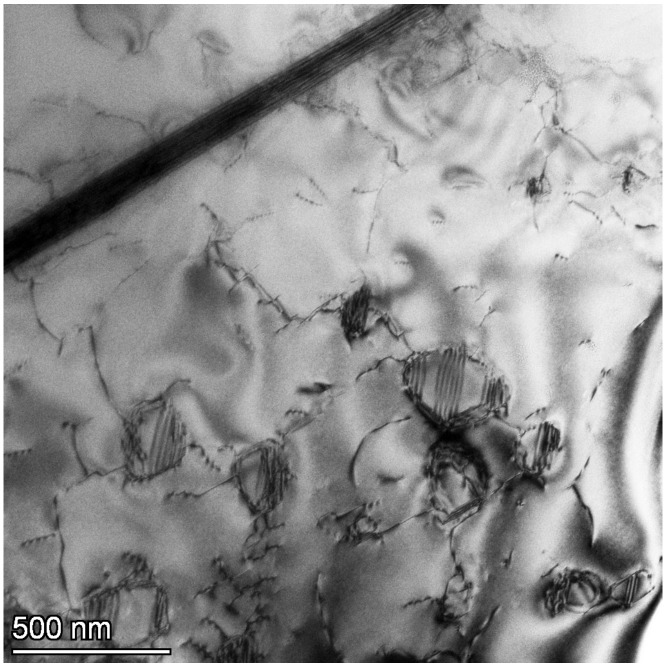

Figure 10. Eta plate and deformation, including stacking faults, in Aged 263, 1073 K and 125 MPa. <200> ***g****.*

Figure 11 shows a different area in the same specimen as Figure 10. Few stacking faults are evident, and the dislocations are almost all in the interfaces and in the matrix, consistent with climb-assisted by-pass. The precipitates are substantially larger than those in the Standard 263, and so interfacial arrays of dislocations begin to appear during deformation.

The determination that creep occurs by climb-assisted by-pass at this temperature is consistent with the DOE-funded work of Shen [11] in a similar alloy (Alloy 282) as well as many other investigators.

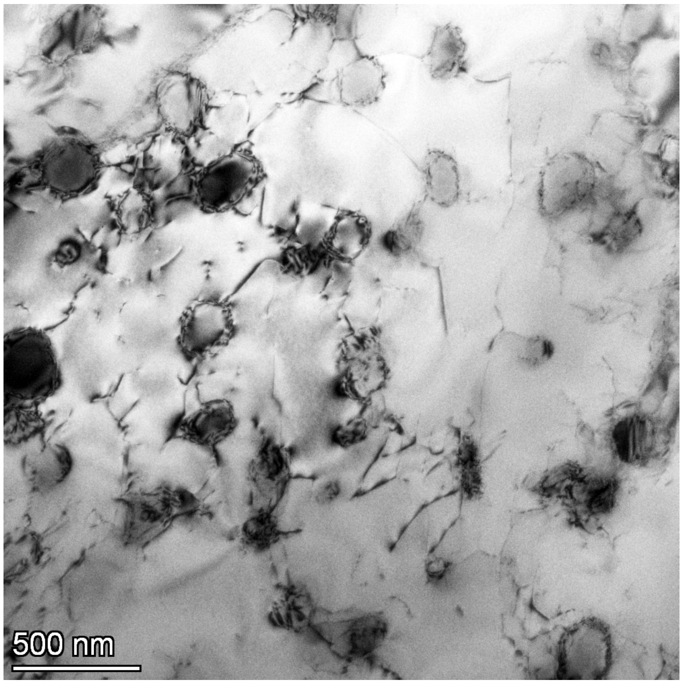

Figure 11. Dislocations mainly in interface and matrix in Aged 263, 1073 K and 125 MPa. <200> ***g****.*

5(b) Intermediate Temperature – 1023 K (750^{o}C)

As the creep temperature dropped to from 1073 to 1023 K, several important trends emerged:

1. The density of stacking faults, which are indicative of <112> partial dislocation shearing, substantially increased in both the Standard and Aged 263 microstructures.
2. Clear evidence of precipitate shearing by standard <110> dislocations, the normal low-temperature deformation mechanism, was found.
3. By-pass was likely also active, indicating that this temperature experienced a combination of all three deformation mechanisms simultaneously: <110> dislocation pair (APB) precipitate shearing, <112> partial dislocation (stacking fault) precipitate shearing, and precipitate by-pass.

First, Figure 12 shows many stacking faults in both the Standard and Aged 263 microstructures. A change at this temperature, especially for the Standard 263 alloy, is the presence of extended stacking faults that traverse multiple precipitates and the matrix continuously. Again, the stacking faults image as the fringe pattern on the {111} slip planes in the micrographs. Note that there are also many traditional dislocations in the matrix, interfaces, and inside the precipitates in all those micrographs. The arrows indicate likely <110> dislocations trapped inside the precipitates, indicative of APB shearing.

The contrast that shows faults appearing, disappearing, and re-appearing in the same band is indicative of partial dislocation shearing on parallel planes. Due to the $\mathbf{g}\cdot\mathbf{R} = 0$ invisibility conditions in brightfield TEM imaging, one superlattice intrinsic stacking fault will show intrinsic contrast, two intrinsic stacking faults directly on top of each other will show extrinsic contrast, and three intrinsic stacking faults directly on top of each other will cancel and appear to have no stacking fault at all. This can be seen by the discontinuities in the faults in all three Standard 263 deformation structures presented in Figure 12.

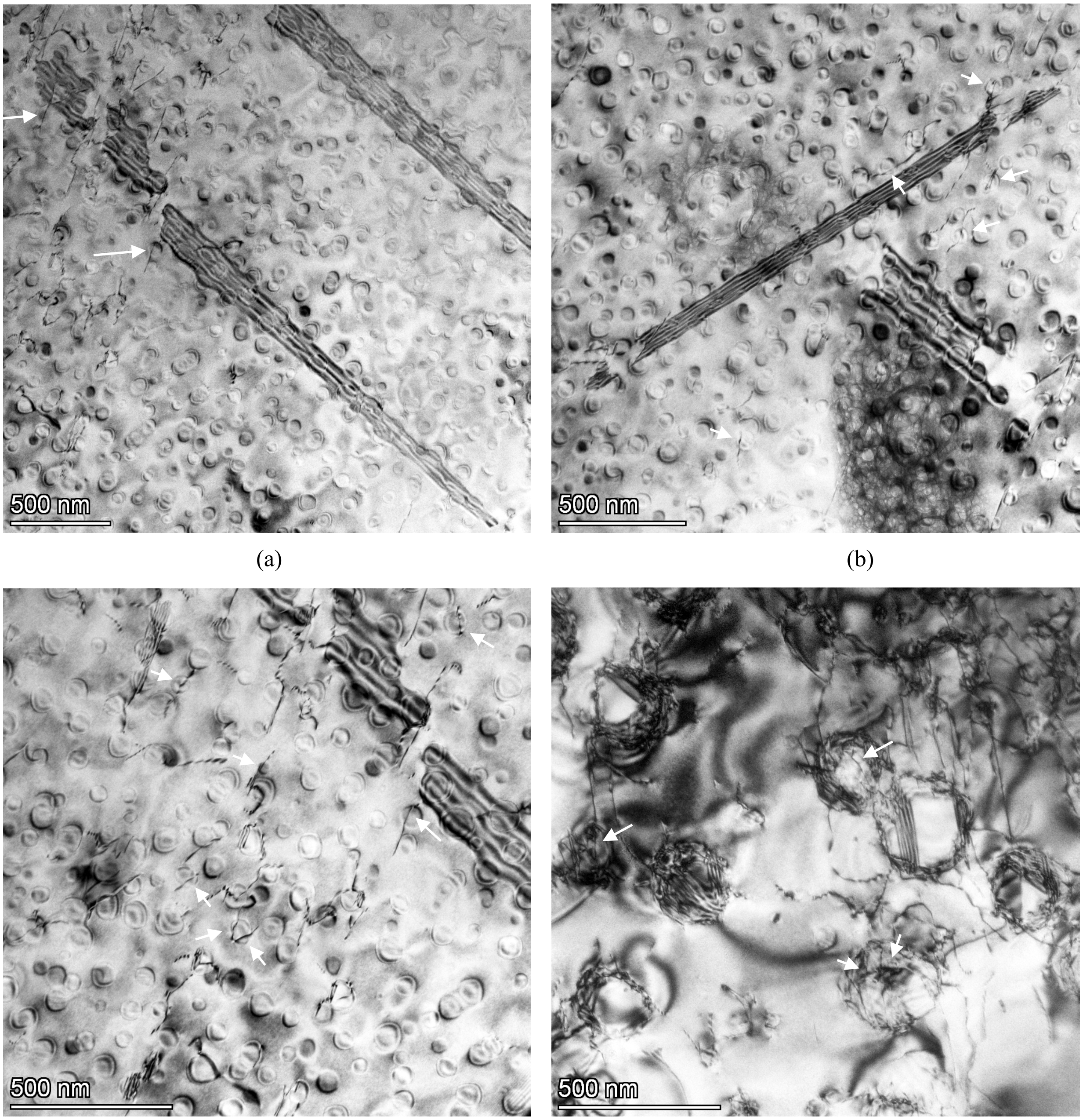

(a) (b)

(c) (d)

Figure 12. Creep deformation microstructures at 1023 K (750ºC). (a) through (c) Standard 263, 1023 K (750ºC), 200 MPa, <111> ***g****. (d) Aged 263, 1023 K (750ºC), 200 MPa, <111>* ***g****. Multiple stacking faults are visible on different planes. In the case of the Standard 263, the faults traverse the matrix and the precipitates. At the arrows, dislocations appear to be trapped inside the precipitates, indicative of traditional APB-shearing by <110> dislocations.*

Figure 13 shows a Standard 263 creep test at 1023 K (750°C) and 150 MPa. At the arrows, it appears relatively clear that <110> dislocations have entered the precipitates and are trapped in the act of shearing when the test failed. In the three cases in the upper left-hand corner, the dislocations are partially in the interface, wrapping around the precipitate, but have evidently penetrated the precipitates partially. They appear to be in the act of thermally-activated shearing.

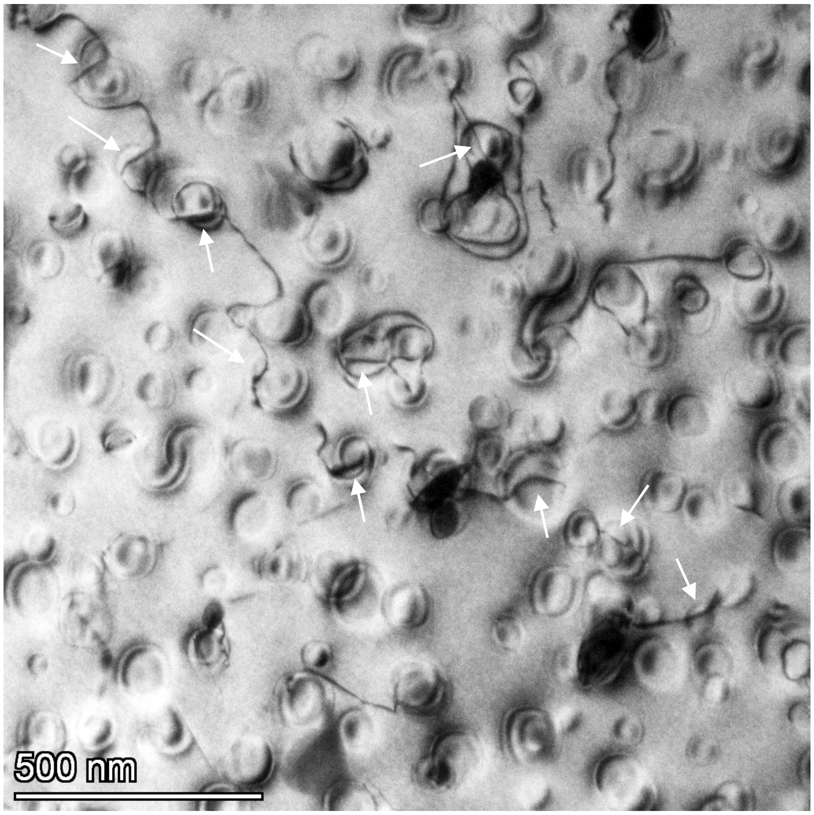

Figure 13. Creep deformation microstructure at 1023 K (750°C), 150 MPa, Standard 263. Arrows indicate areas where <110> dislocations appear to have penetrated precipitates, indicating APB shearing. <111> ***g***.

Finally, Figure 14 once again shows an η plate apparently acting as a dislocation source for the a γ matrix, with loops bowing out from the interface into the matrix, potentially improving the creep ductility of the alloy.

This temperature is often in the transition from shearing to by-pass, with stacking fault-related deformation as well.

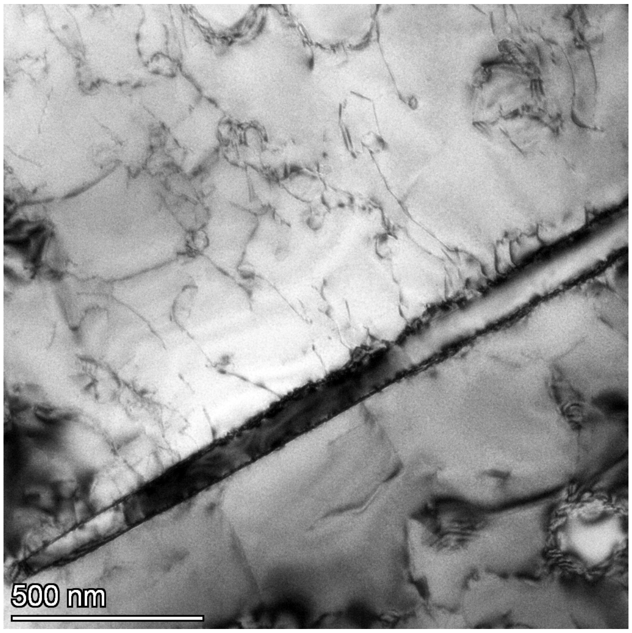

Figure 14. Creep deformation microstructure at 1023 K (750ºC), 200 MPa, Aged 263. <111> ***g****. An η plate (running diagonally across the micrograph) appears to be a potent source of matrix dislocations, which are bowing out from the interface into the matrix.*

TEM studies of the η alloy revealed similar behavior, with the η plate interface acting as a dislocation source for the matrix. Figure 15 shows an η plate containing a network of interfacial dislocations after creep at 1023 K. The interface is, therefore, semi-coherent, and these interfacial dislocations can bow out into the matrix as shown in Figure 16.

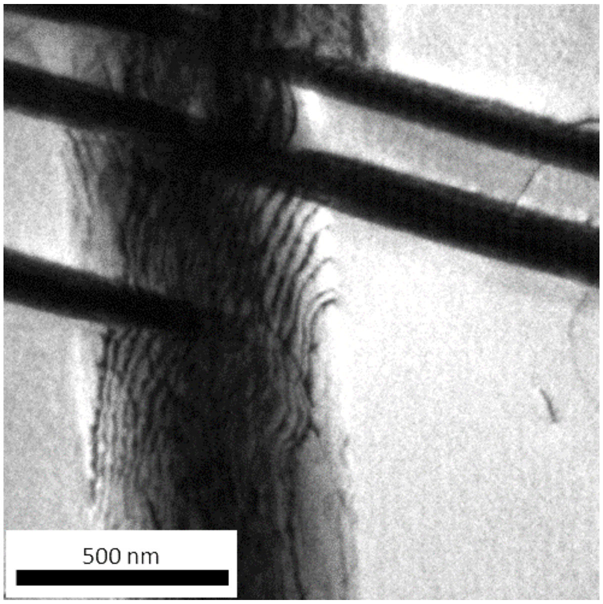

Figure 15. Creep deformation microstructure at 1023 K (750ºC), η alloy. The three plates running horizontally across the micrograph are inclined substantially, while the one that is running vertically from top to bottom is flatter and almost in the plane of the photo. An interfacial dislocation network is clearly visible. Under different diffraction conditions, dislocations are visible which are perpendicular to those visible here.

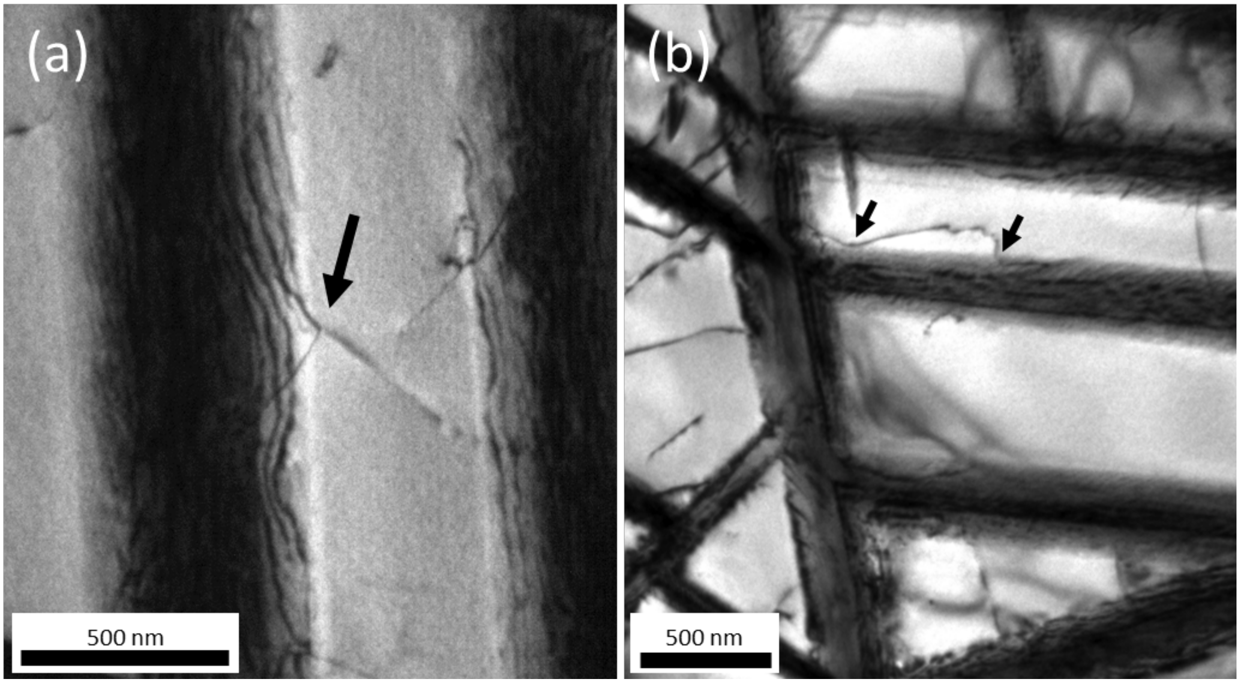

Figure 16. Creep deformation microstructure at 1023 K (750ºC), η alloy. Matrix dislocations bowing into the matrix (a) connected to an interfacial node (arrow) on one side and (b) from the interfacial network, attached on both sides (arrows).

5(c) Lowest Temperature – 973 K (700ºC)

As the creep temperature was reduced to 973 K, the density of stacking faults was also reduced. γ' shearing by traditional <110> dislocations became the most common mechanism, consistent with the literature results for similar alloys.

Consistent with the higher temperatures, in the Aged 263 alloy, the η plates appeared to be potent dislocation sources, as shown in Figure 17. Also, dislocation debris is observed inside the precipitates (arrows), which is indicative of APB-based shearing, and which is consistent with the literature for similar alloys.

Figure 17. Creep deformation microstructure at 973 K (700ºC), 325 MPa, Aged 263. <200> ***g****. An* η *plate (running almost vertically) appears to be a potent source of matrix dislocations, which are bowing out from the interface into the matrix. Note the fine (~ 30 nm diameter)* γ' *particles that precipitated during creep.*

A final observation, which may be seen in Figure 17 and at higher resolution in Figure 18, is that fine γ' precipitates formed during creep of the Aged 263 alloy at 973 K. Since the solubility of both γ' and η is significantly higher at the aging temperature of 1123 K than at the creep temperature of 973 K, this is not a surprise. ThermoCalc modeling verified that γ' precipitation is expected. Some fine precipitation was also observed at 1023 K during creep.

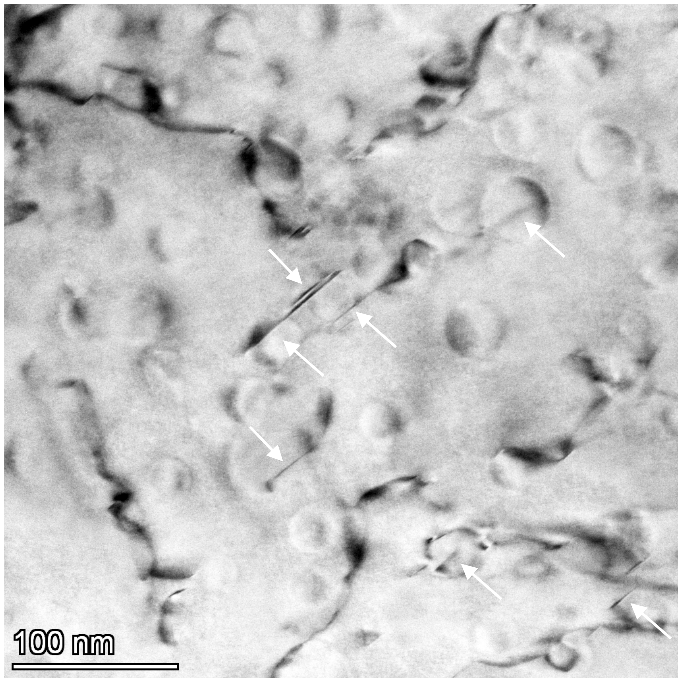

Figure 18. Creep deformation microstructure at 973 K (700^{o}C), 325 MPa, Aged 263. <200> ***g****.* γ' *precipitated during creep with a particle size of around 30 nm. APB-based shearing appeared to be the dominant deformation mechanism. Dislocation debris inside the precipitates, indicative of APB shearing, is indicated at the arrows.*

5(d) Summary of Creep Deformation Mechanisms

- Creep deformation is dominated by climb-assisted by-pass at 1073 K (800^{o}C) in both Traditional and Aged 263 at all stresses tested in this study.
- Creep deformation is dominated by <110> (APB) dislocation shearing at 973 K (700^{o}C) in both Traditional and Aged 263 at all stresses tested in this study.
- Creep deformation occurs by a combination of <110> APB shearing, <112> stacking fault shearing, and likely climb-assisted by-pass at 1023 K (750^{o}C) in both Traditional and Aged 263.
- In Aged 263, the η/γ interface appears to be a potent source of matrix dislocations, which might improve creep ductility due to a high mobile dislocation density and a reduction in the γ' volume fraction near the grain boundaries (where η precipitation is maximized). This is also observed very clearly in the η alloy, where interfacial dislocation networks produced mobile dislocations in the matrix.

6. Results – Creep Modeling

Physically-based creep models for nickel-base superalloys, especially in the regime where climb-assisted by-pass of the precipitates is the dominant mechanism, have been in development for decades. A representative model which has been well-received was developed by Dyson's group [12]. Shen [11] modified it to successfully model the creep behavior of Alloy 282, which is similar to 263.

Dyson's formulation of the creep strain rate is:

$$\dot{\epsilon} = \rho A f(1-f)\left(\sqrt{\frac{\pi}{4f}} - 1\right)\sinh\left(\frac{C(\sigma_{total})b^2\lambda}{MkT}\right) \qquad (1)$$

Where $\dot{\epsilon}$ is the strain rate, ρ is the dislocation density, A and C are fitted coefficients, f is the γ' volume fraction, b is the Burgers vector, λ is the particle spacing, M is the Taylor factor, k is the Boltzmann constant and T is the temperature in Kelvin. σ_{total} is calculated by subtracting back stress (climb or shearing depending on the dominant mechanism) from applied stress:

$$\sigma_{total} = \sigma_{app} - \sigma_b - \sigma_0 \qquad (2)$$

where σ_{app} is the applied stress, σ_b is the back stress, and σ_o is a threshold stress that is interpreted to come from dislocation forest hardening [13]:

$$\sigma_0 = 0.25 M G_T b\sqrt{\rho} \qquad (3)$$

where M is the Taylor factor, $G_T = E_T/2(1+\nu)$ is the shear modulus, b is the Burgers vector and ρ is the dislocation density. The mean free path is:

$$\lambda_t = 1.6\, p_t\left(\sqrt{\frac{\pi}{4f}} - 1\right) \qquad (4)$$

where p_t and f are the γ' particle size and volume fraction, respectively.

The model is formulated such that the strain rate is zero if σ_{total} is equal to zero or is negative, and it is equal to Equation 1 if the σ_{total} is positive. A negative σ_{total} would imply that the applied stress is less than the sum of the back stress + threshold stress, so no creep would be expected.

The back stress depends on the deformation mechanism. In the original formulations, climb-assisted by-pass was assumed at higher temperatures. There is some physics related to kink density and diffusion during climb in the formulation of the back stress, which takes the following form in the steady-state regime [12]:

$$\sigma_{b\,(climb)} = \left(\frac{2f}{1+2f}\right)\sigma_{app} \qquad (5)$$

In the case of precipitate shearing, the back stress will not be related to jogs and climb, but instead would result from resistance to shearing. Strictly speaking, the formulation of the Dyson model would not be completely consistent with simply changing the back stress, but Shen did so successfully, and the result is still a phenomenological model informed by material and microstructure. The back stress during shear takes the following form [11, 14]:

$$\sigma_{b\ (shear)} = \frac{\gamma_{APB}}{2b}\left[\left(\frac{12\gamma_{apb}fp}{\pi G b^2}\right)^{\frac{1}{2}} - f\right] \qquad (6)$$

where γ_{APB} is the γ' anti-phase boundary energy, p is the particle size, b is the Burgers vector, f is the gamma prime volume fraction, and G is the shear modulus. This is only appropriate when shearing is occurring by APB-coupled pairs of ½<110> dislocations.

The precipitate size increases during creep, and this can be taken into account by making the precipitate size a function of time instead of a constant with classical Ostwald ripening:

$$p_t = (R_0^3 + kt)^{\frac{1}{3}} \qquad (7)$$

where p_t is the gamma prime particle size at a given time t, R_0 and k are fitted coefficients for a given temperature, and t is the time in hours. The values of R_0 and k for each temperature were obtained by cubic fitting particle size data generated from long-term aging experiments at the temperatures of the creep tests.

Equations 1 through 7 form the basis of the creep model, using Equation 5 to generate a climb-assisted by-pass prediction or Equation 6 to generate a shearing prediction. All the constants in the equations are microstructural parameters or material parameters that are available except for three: the fitting coefficients A and C, and the dislocation density, ρ. A is based on a combination of jog density and self-diffusivity of nickel. Over the temperature region in our study, the self-diffusivity of nickel changes by less than 1%. Therefore, A is kept constant across all materials for all stress-temperature combinations. C is a unitless parameter. Dislocation density is also treated as a fitted parameter that changes with stress-temperature combinations. Values for dislocation density were qualitatively derived from TEM studies.

Shen assumed that the dislocation density of Alloy 282 at steady state was independent of temperature and stress, and he used a best-fit to estimate that value. Based on the varying deformation mechanisms presented earlier, and the observation that the dislocation density would be expected to increase at higher stresses, we allowed the dislocation density to be used as a fitting variable along with A and C.

Bayesian optimization was utilized to generate the constants. The procedure was as follows:

1. The initial model was calibrated using the Standard 263 test data at 1073 K (800°C) in the climb-assisted by-pass regime. This is the regime that is most consistent with Dyson's work. Based on Shen's work and qualitative TEM studies, dislocation densities were selected for the three stresses available. (The 145 MPa test had an experimental error that resulted in an apparent negative creep rate, so it was excluded from the analysis.). Bayesian optimization was done to obtain a best fit for the constants A and C based on these three tests.
2. These values of A and C were kept constant for all other tests, including the Standard and Aged 263 at all stresses and temperatures.

3. In the case of the Aged 263, the γ' volume fraction and size were substantially different than the Standard 263 due to the formation of η. These microstructural parameters were entered in the model. **This is how the effect of η is handled in our model; it is not explicitly included, but it affects creep rates because the formation of η during aging reduced the γ' volume fraction and increased its size.** In the case of the Aged 263, we used the same dislocation densities that were optimized for the Standard 263 alloy. Thus, A, C and ρ were the same at a given stress for both the Aged and Standard 263. If we allowed different ρ's we could fit the data almost perfectly, but this would be simply curve-fitting and not modeling. Having said that, it is certainly possible that different values of dislocation densities might occur in the Standard and Aged 263 at the same stress and temperature, because the microstructures are so different.
4. For all temperatures and stresses, we attempted to fit both a by-pass model and a shearing model.
5. Primary and tertiary creep were removed from the experimental data in order to just fit secondary creep.
6. A python-based program with a user-friendly GUI was used to develop the curves, and this is publicly available at the link in the "Outcomes from this Research" section later. It is easy to change all important material parameters, as well as test parameters, to do virtual experiments. The model can also be used to generate a full creep curve if enough information is available for damage evolution which drives the onset of tertiary creep.

6(a) Highest Temperature – 1073 K (800°C)

Figure 19 shows model predictions vs experiment for three tests conducted at 1073 K, after removing primary and tertiary creep from the experimental data. Since the model was calibrated with the Standard 263 data, and we are only trying to fit a single slope, it is no surprise that the Standard 263 model matches the data almost perfectly at all three stresses.

The interesting results are those for the Aged 263. Recall that all three fitting constants, A, C and the dislocation density were kept constant for both the Standard and Aged 263. The differences in the model predictions are due to a reduced γ' volume fraction and increased γ' size that resulted from aging and the formation of η at the expense of the γ'. It was assumed that there was no strengthening from the η, since the creep model is based on by-pass of spherical γ' precipitates. At the lowest stress of 100 MPa, the agreement between the model and the data is actually quite good. The specimen crept slightly faster than predicted, within 25%. As the stress increased, the model fit worsened, with the specimen creeping increasingly faster than the model prediction as the stress increased.

The difference in creep rates between the model and the experiment for the Aged 263 was approximately a factor of 5 at 125 MPa and factor of 15 at 250 MPa. Potential mechanisms will be discussed later in this section.

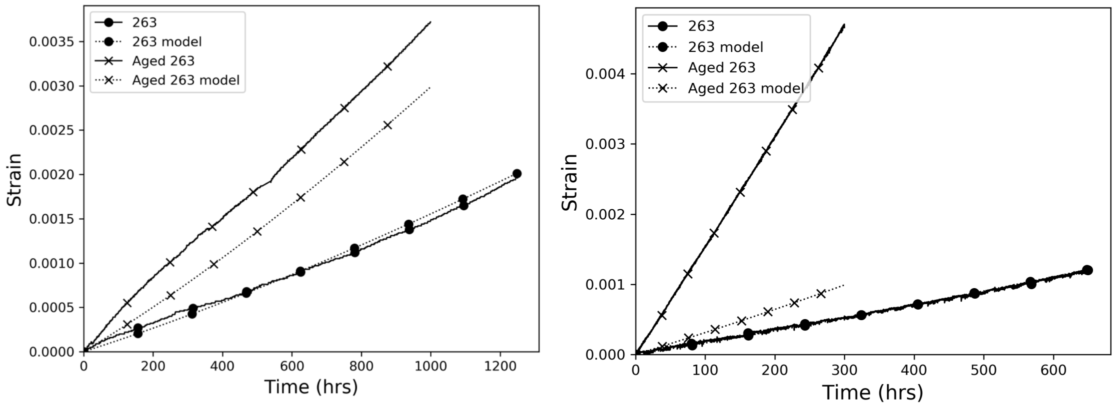

1073 K, 100 MPa, by-pass model

1073 K, 125 MPa, by-pass model

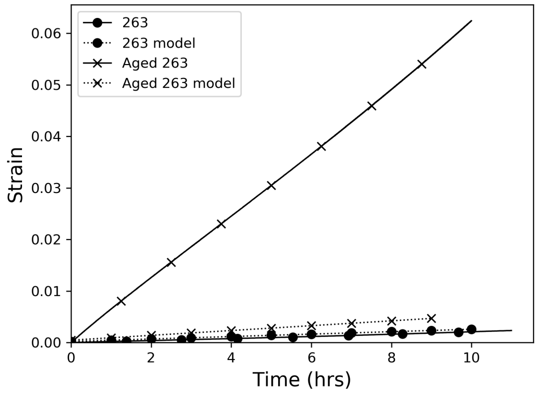

1073 K, 250 MPa, by-pass model

Figure 19. Steady-state creep curves and model predictions at 1073 K (800ºC).

6(b) Lowest Temperature – 973 K (700ºC)

At 973 K, deformation occurs via precipitate shearing, as demonstrated in Section 5. Unsurprisingly, trying to apply the by-pass model to the Standard and Aged 263 was not successful at modeling even the Standard 263 alloy. However, applying the shearing model with Equation 6 for the back stress instead of Equation 5 worked much better.

Figure 20 shows model predictions vs experimental data for the two stresses tested at 1073 K, after removing primary and tertiary creep from the experimental data. A and C were identical to the by-pass model, and dislocation density was optimized on the Standard 263 as a fitting parameter. The same value of optimized dislocation density was used for the Aged 263, along with the same A and C. In this case, the fit is quite good at both stresses. Again, the Standard 263 data fits almost exactly, and the Aged 263 creeps slightly faster than predicted by the shearing-based creep model at 400 MPa and fits almost exactly at 325 MPa.

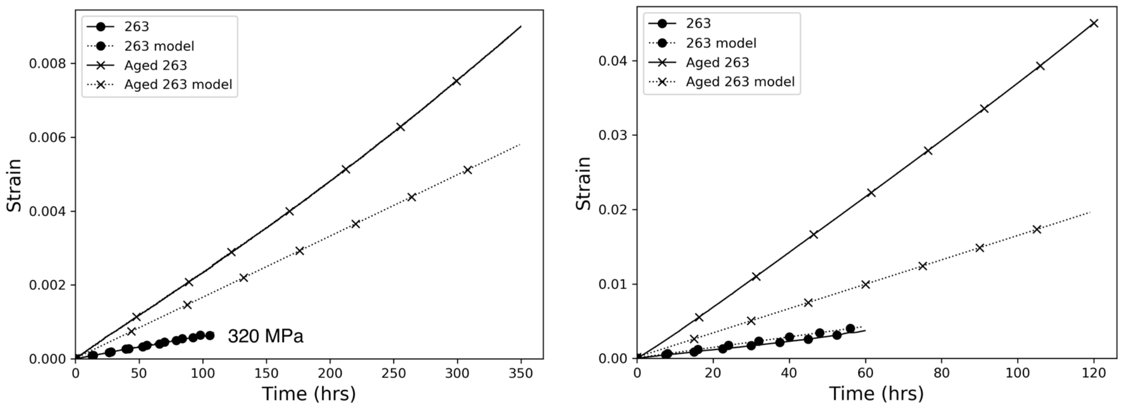

973 K, 325 MPa, shearing model

973 K, 400 MPa, shearing model

Figure 20. Steady-state creep curves and model predictions at 973 K (700°C).

The Aged 263 specimen creep rates exceeded the model predictions by a factor of 1.5x at 325 MPa MPa and 2.3x at 250 MPa. Potential mechanisms will be discussed later in this section.

6(c) Intermediate Temperature – 1023 K (750°C)

At 1023 K, substantial increases in stacking faults and <112> partial dislocation precipitate shearing were observed, as demonstrated in Figure 5. Similar to 973 K, the by-pass model was not able to successfully predict the Standard 263 curves. Unsurprisingly, trying to apply the by-pass model to the Standard and Aged 263 was not successful. The shearing model fit better, as shown in Figure 21. However, there is strong evidence that this fit is not physically consistent, as discussed below.

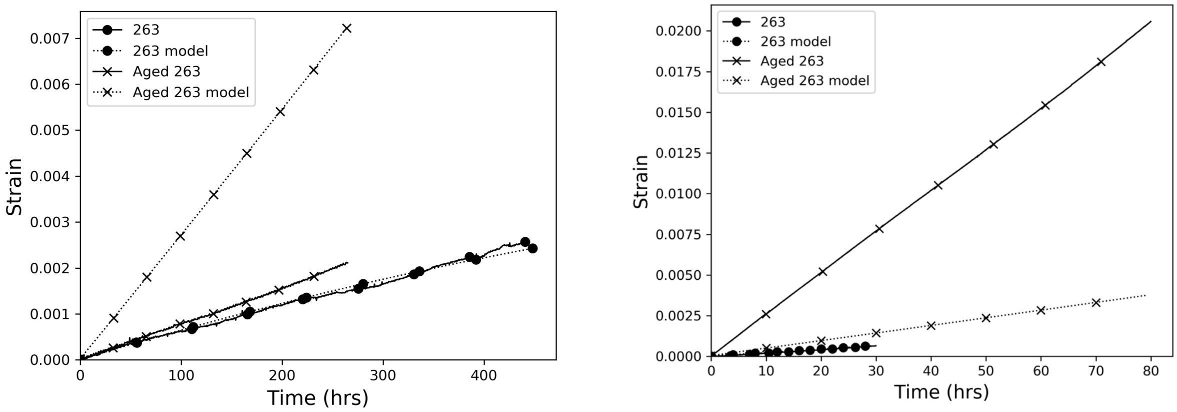

1023 K, 200 MPa, shearing model

1023 K, 300 MPa, shearing model

Figure 21. Steady-state creep curves and model predictions at 1023 K (750°C).

Since our approach is to keep A and C constant at all temperatures and stresses, the only fitting parameter available after initial model calibration is the steady-state dislocation density. At 973 and 1073 K, across two different mechanisms of shearing (973 K) and by-pass (1073 K), the fitted values of dislocation density were reasonable, and the density increased with increasing stresses, as one would expect. However, this was not the case at 1023 K. The only way to get a good fit for the Standard 263 was to have a lower dislocation density at 300 MPa than at 200 MPa. This results in the curves shown in Figure 21, but is not physically reasonable or justifiable. Further, for the Aged 263, the direction of the discrepancy between the model and the data flips between 200 and 300 MPa. At 200 MPa, the observed creep rate is substantially lower than predicted by the model, while at 300 MPa it is substantially higher. The model that worked at 973 K clearly failed at 1023 K, and the by-pass model did not fare any better. Possible reasons for this are discussed below.

6(d) Discussion – Creep Models

The best performance of the model was at 973 K in the precipitate shearing regime. The Standard 263 was able to be fit exactly with the same A and C that were optimized by the by-pass model at 1073 K. The Aged 263 model predictions were within around a factor of two of the data, with the alloy always creeping slightly faster than the model predictions. The Aged 263 always crept faster, because the changes in the back stress (Equation 6) due to the reduction in precipitate volume fraction.

The model assumes that the remaining γ' after aging is uniformly distributed with a constant average particle size. As shown in Figure 3, this is not exactly accurate. The η precipitates in the grain boundaries and cannibalizes the γ' locally. This results in a quasi-composite structure with a grain boundary "phase" that is mostly η and matrix, and a grain core "phase" that has a higher volume fraction of γ'. Additionally, as discussed in Figures 17 and 18, some fine γ' precipitated during creep, and this bi-modal distribution of γ' was ignored in the model. All things considered, a factor of two difference in creep data and modeling is quite good.

The second-best performance of the model was at 1073 K in the by-pass regime. Again, the Standard 263 was fit perfectly, but this is no surprise because the model was calibrated with this data and we are only trying to fit one scalar performance variable (steady-state creep rate).

For the Aged 263 at 1073 K, the fit was fairly good at the lowest stress of 100 MPa, within 25%. As the stress increased from 100 MPa to 125 MPa to 250 MPa, the discrepancy in the predicted and observed creep rates increased from 25% to a factor of 5 to a factor of 15. Again, the specimens all crept faster than the model predictions.

This clearly indicates that the model is not capturing the physical situation completely, and it is likely related to microstructure. The model assumes that dislocations glide easily across the matrix, then they encounter a γ' precipitate, get stuck, and slowly climb/glide up around the precipitates which are fairly closely-spaced. In the Aged 263, the grain boundary phase has no γ'. Also, as discussed at length in Section 5, the η plates are very rich sources of matrix dislocations during creep. Therefore, we now have a grain boundary "phase" that is mainly a soft matrix and a rich source of matrix dislocations that can easily glide. This combination is completely consistent with an increased creep rate compared to the Standard N263 microstructure. Some initial modeling was attempted to try to treat this as a composite of an overaged N263 grain core and an η alloy grain boundary. Further research is ongoing to try to explore this in more detail.

So, both 973 K and 1073 K can be modeled reasonably well with our modeling approach taken a little bit further. 1023 K, however, cannot be modeled. As discussed earlier, the only way to make the data fit the Standard 263 is to have the dislocation density ***decrease*** as stress ***increases***. This is not supportable. Further, the sign of the misfit between the model and the data switched between 200 and 300 MPa. The modeling approach cannot be salvaged for this temperature.

There are two probable reasons for this. First, it is likely that there is some combination of shearing and by-pass at this temperature. Second, and more importantly, the shearing deformation mechanism changed from the <110> APB-coupled dislocation pairs (which are the heart of the model) to also include substantial shearing by <112> stacking fault-related partial dislocations. The back stress in the shearing model is based on APB-based shearing, so it would be very surprising if it could model the <112> partial dislocation shearing. A completely new model, with at minimum a completely new formulation of the back stress would be required.

It has been known for at least 40 years that superalloys start to creep by <112> partial shear at around 1400ºF (760ºC) which was a common creep test temperature. In recent years, Mike Mills' group at Ohio State has made tremendous progress in understanding the actual rate-dependent mechanisms, which turn out to include a diffusing Cottrell atmosphere of cobalt in the precipitates [15-16, for example]. This would seem to be a fruitful area to explore in order to develop a new physically-based creep model for 1073 K.

It is actually satisfying to find that a physically-based model can't be made to work if the mechanism is wrong! This also lends some confidence that the more successful modeling at 973 and 1073 K really is more than just "advanced curve fitting."

7. Products of this Research

Publications

N.R. Mohale, P.G. Sanders, J.P. Shingledecker, W.W. Milligan: "Effects of Eta Phase on Creep Performance of the Nickel-Base Superalloy 263", *Materials Science and Engineering A*, in final stages of preparation, to be submitted.

N.R. Mohale, W.W. Milligan, P.G. Sanders, C.L. White, J.P. Shingledecker and P.A. Bridges: "Effects of Eta Phase on Creep Performance of the Nickel-Base Superalloy 263", in "Proceedings of the Joint EPRI-HiMat 123 Conference on Advances in High Temperature Materials," Nagasaki, Japan, October 20-24, 2019, J. Shingledecker and M. Takeyama, eds., ASM International, Materials Park, OH, pp. 621-627.

W.W. Milligan, P.G. Sanders, C.L. White, J.P. Shingledecker, and D.F. Purdy, "Design, Creep Performance and Deformation Behavior of an ETA-Phase Strengthened Nickel-Base Alloy for A-USC Power Plant Applications," in "Proceedings from the Eighth International Conference on Advances in Materials Technology for Fossil Power Plants", J. Shingledecker, J. Parker and J. Siefert, eds., ASM International, Materials Park, OH, 2016, pp. 202-212.

Presentations

Mohale was scheduled to present at the TMS Annual Meetings in 2020 in San Diego and 2021 in Orlando, but both were canceled due to COVID.

Mohale presented results at the DOE Crosscutting Technologies Program Review Meetings, annually from 2018-2019. Milligan presented in 2017 on behalf of the first student who left the program, and the meeting in 2020 was canceled due to COVID.

Sanders presented results at the Joint EPRI-HiMat 123 Conference on Advances in High Temperature Materials, Nagasaki, Japan, October 21, 2019.

Mohale presented results at the TMS Annual Meeting in San Antonio, Texas, March 12, 2019.

Milligan presented results at the 18th International Conference on the Strength of Materials in Columbus, OH on July 17, 2018.

Milligan presented results at the EPRI Eighth International Conference on Advances in Materials Technology for Fossil Power Plants in Albufeira, Portugal, October 11, 2016.

Software and Supporting Data

The python-based creep model software and the supporting data and micrographs for the program are publicly available at:

https://digitalcommons.mtu.edu/all-datasets/5/

7. Summary and Conclusions

In order to study the effects of η precipitation on the creep performance of a typical nickel-base superalloy, the material was aged at 1123 K for 1,000 hours prior to creep testing. This Aged 263 microstructure was compared to Standard 263, and an alloy developed at Michigan Tech that contained only η. The Aged 263 contained η in and near the grain boundaries, along with a reduced volume fraction of γ' and an increased γ' precipitate size.

The creep resistance of the Standard 263 was superior in all cases, with the exception of creep ductility, which was substantially enhanced in both the Aged 263 and the η alloy. Transmission Electron Microscopy determined that the η plate interfaces contain a network of interfacial dislocations that are rich sources of matrix dislocations during creep. This allows an increased dislocation density near the grain boundaries during creep, in areas that are denuded in γ' due to the η precipitation, which would allow an increased creep ductility and, in some cases, an elevated creep rate.

Transmission Electron Microscopy studies determined that the dominant deformation mechanisms during creep were: climb-assisted precipitate by-pass at 1073 K; precipitate shearing by traditional APB-coupled <110> dislocations at 973 K; and a combination of APB shearing and stacking fault related <112> partial dislocation shearing at 1023 K, possibly mixed with some by-pass in this transition temperature regime.

A Dyson-type creep model was used to fit the creep data. The η is not accounted for explicitly, but instead comes in through a reduction in the γ' volume fraction and an increase in its size during aging. The model was very successful at capturing the behavior of the Standard 263 and the Aged 263 in the shearing regime at 973 K using an APB-shearing back stress, and was moderately successful at capturing the behavior of Standard 263 and Aged 263 at 1073 K in the by-pass regime using a by-pass back stress. At higher stresses at 1073 K, the model predictions worsened for the Aged 263 worsened, likely due to increasing matrix dislocation density and motion near the grain boundaries, promoted by the η plate interfacial dislocation sources. This same mechanism likely contributed to accelerated creep rates and increased creep ductility.

The model failed completely at 1023 K, consistent with the change in shearing mechanism from traditional <110> APB shearing to add <112> partial shearing with stacking faults. At minimum, the existing formulations for back stress would need to be modified to handle this. It is also possible that a completely new modeling approach may be necessary, based on recent work that found long range diffusion of cobalt and other elements ahead of partial dislocations shearing precipitates during creep at this temperature.

8. References

[1] Shingledecker, J.P. and Pharr, G.M., “The Role of Eta Phase Formation on the Creep Strength and Ductility of INCONEL Alloy 740 at 1023 K (750 C),” *Metall. Mater. Trans. A,* Vol. 43A (2012), pp. 1902-1910.

[2] Unocic, K.A., Shingledecker, J.P. and Tortorelli, P.F., “Microstructural Changes in Inconel® 740 After Long-Term Aging in the Presence and Absence of Stress” *JOM*, vol. 66 (12) (2014), pp. 2535-2542.

[3] Zhang, Y.H. and Knowles, D.M., “Prestraining Effect on Creep Behaviour of Nickel Base C263 Superalloy”, *Mater. Sci. Tech*., vol. 18 (2002), pp. 917-923.

[4] Zhao, J.C., and Henry, M.F., “The Thermodynamic Prediction of Phase Stability in Multicomponent Superalloys”, *JOM*, vol. 54(1) (2002), pp. 37-41.

[5] Zhao, S., Xie, X., Smith, G.D., and Patel, S.J.. “Microstructural Stability and Mechanical Properties of a New Nickel-Based Superalloy”, *Mater. Sci. Engr A*, vol. 355(1) (2003), pp. 96-105.

[6] Evans, N.D., Maziasz, P.J., Swindeman, R.W. and Smith, G.D., “Microstructure and Phase Stability in Inconel Alloy 740 During Creep”, *Scripta Mater*., vol. 51 (2004), pp. 503-507.

[7] Shingledecker, J.P., Evans, N.D. and Pharr, G.M., “Influences of Composition and Grain Size on Creep–Rupture Behavior of Inconel® Alloy 740”, *Mater. Sci. Eng. A*, vol. 578 (2013), pp. 277-286.

[8] Wong, M.J., Sanders, P.G., Shingledecker, J.P. and White, C.L., “Design of an Eta-Phase Precipitation-Hardenable Nickel-Based Alloy with the Potential for Improved Creep Strength Above 1023 K (750° C),” *Metall. Mater. Trans. A,* Vol. 46A (2015), pp. 2947-2955.

[9] Milligan, W.W., Sanders, P.G., White, C.L., Shingledecker, J.P. and Purdy, D.F., “Design, Creep Performance and Deformation Behavior of an ETA-Phase Strengthened Nickel-Base Alloy for A-USC Power Plant Applications,” in *“Proceedings from the Eighth International Conference on Advances in Materials Technology for Fossil Power Plants”*, Albufeira, Portugal, J. Shingledecker, Parker, J. and Siefert, J., eds., ASM International, Materials Park, OH, 2016, pp. 202-212.

[10] Zhao, J.C., Ravikumar, V., and Beltran, A.M., “Phase Precipitation and Phase Stability in Nimonic 263”, *Metall. Mater. Trans. A*, vol. 32(6) (2001), pp. 1271-1282.

[11] C. Shen, “Modeling Creep-Fatigue-Environment Interactions in Steam Turbine Rotor Materials for Advanced Ultra-supercritical Coal Power Plants”, DOE-NETL Cooperative Agreement DE-FE0005859, Final Technical Report, April 2014.

[12] Dyson, B. F., “Microstructure based creep constitutive model for precipitation strengthened alloys: theory and application”, *Mat Sci. Tech.,* vol. 25, (2009), pp. 213-220.

[13] Kassner, M. E. and Pérez-Prado, M. T. *“Fundamentals of Creep in Metals and Alloys”,* Elsevier Science Ltd, 2004.

[14] Reed, R. C. *"The Superalloys, Fundamentals and Applications",* Cambridge University Press, 2006.

[15] Viswanathan, G.B., Shi, R., Genc, A., Vorontsov, V.A., Kovarik, L., Rae, C.M.F., and Mills, M.J., "Segregation at stacking faults within the gamma prime phase of two Ni-base superalloys following intermediate temperature creep", Scripta Materialia, vol. 94, (2015), pp. 5-8.

[16] Smith, T.M., Rao, Y., Wang, Y., Ghazisaeidi, M., and Mills, M.J., "Diffusion processes during creep at intermediate temperatures in a Ni-based superalloy", *Acta Materialia*, vol. 141, (2017), pp. 261-272.